

First-principles characterization of the electronic and optical properties of hexagonal LiIO_3



B. Van Troeye, Y. Gillet, S. Poncé*, X. Gonze

Université catholique de Louvain, Institute of Condensed Matter and Nanosciences, European Theoretical Spectroscopy Facility, NAPS Chemin des étoiles 8, bte L07.03.01, B-1348 Louvain-la-Neuve, Belgium

ARTICLE INFO

Article history:

Received 14 March 2014

Accepted 2 April 2014

Available online 9 May 2014

Keywords:

Density functional theory

Lithium iodate

Cell optimization

Phonon modes

Macroscopic dielectric permittivity

Nonlinear properties

ABSTRACT

Within the density functional theory framework, we investigate the structural, electronic, vibrational, dielectric, piezoelectric and optical properties of hexagonal lithium iodate, including some nonlinear response properties, like the nonlinear dielectric (electronic) susceptibility, the electro-optic tensor and the Raman tensor. Beyond the comparison with available experimental data and the associated analysis, we predict the values of several properties or characteristics of this material, e.g. the phonon frequencies with B symmetry, that are silent in both IR and Raman experiments, the Born effective charges, for which a detailed analysis is performed, Raman susceptibilities and the decomposition of the clamped electro-optic tensor in terms of the different modes. The agreement with available experimental results is reasonable to excellent, depending on the property. The lattice parameters and macroscopic dielectric constants agree to the experimental ones within 2%. The Kohn–Sham electronic bandstructure is predicted, but suffers from the well-known DFT band gap problem. Reflectivity spectra computed with the density functional perturbation theory are in qualitative and quantitative agreements with experiments for incident light along the two main hexagonal axes. The phonon frequencies at the Brillouin zone center are, in average, 5.74% apart from the experimental one. The previous assignment of Raman features is discussed, on the basis of our computed Raman spectra, including relative peak heights. Finally, this study confirms theoretically the large nonlinear coefficients d_{31} and d_{33} of -6.6 pm/V and -7.5 pm/V as well as its noteworthy piezoelectric and electro-optic properties that make this material remarkable.

© 2014 Elsevier B.V. All rights reserved.

1. Introduction

The lithium iodate (LiIO_3) crystal features a wide transparency range and important nonlinear coefficients (around -7 pm/V), acousto-optical and piezoelectric properties along with an easiness in the growth process [1]. This crystal is used for generation of 347 nm light by Second Harmonic Generation (SHG) of ruby lasers [2], for generation of 532 nm light by SHG of Ruby/Nd:YAG lasers [3,4] and for piezoelectric sensors [5] but its highly hygroscopic nature requires protection from moisture. LiIO_3 crystallizes into two thermodynamically stable phases at room temperature: an hexagonal closed packed α -phase that belongs to the $P6_3$ space group [6,7] and a tetragonal β -phase with the $P4_2/n$ space group [8,9]. The LiIO_3 crystal undergoes a phase transition from the α -phase to an orthorhombic phase at 520 K [10].

This first-principles study is focused on the hexagonal α -phase because of its interesting optical properties: its large birefringence

allows broad phase matching for SHG applications while its second harmonic nonlinear coefficient d_{31} is comparable to the typical LiNbO_3 nonlinear reference crystal [11].

Hexagonal LiIO_3 has been previously studied experimentally for its optical properties: the measured dielectric permittivities along the hexagonal a and c axes are respectively 3.61 and 3.06. The contribution of the lattice dynamic to the static permittivity is weak $\epsilon_{11}^0 = 8.2$ and $\epsilon_{33}^0 = 6.4$ with respect to other materials such as LiNbO_3 show little contribution of the lattice to the static permittivity [12]. The nonlinear coefficients d_{31} and d_{33} of the crystal have also been deeply analyzed with an important scattering of values ranging from 3.9 to 7.31 pm/V for d_{31} and from 3.9 to 4.6 pm/V for d_{33} [13–17].

In contrast to the numerous experimental studies, there have been very few theoretical studies of the LiIO_3 crystal. Let us mention in particular the recent theoretical study by Gang et al. [18] within the Density Functional Theory (DFT) [19] framework using the Generalized Gradient Approximation (GGA) [20] and Hamann norm-conserving pseudopotentials [21] to model the electron–ion interaction. They have investigated the structural and optical properties of hexagonal LiIO_3 . In the present study,

* Corresponding author. Tel.: +32 10473630.

E-mail address: samuel.pon@gmail.com (S. Poncé).

we use a similar level of theory and approximation for cell relaxation and total energy determination but we also study the lattice vibrations, nonlinear and electro-optic coefficients, the reflectivity and Raman spectra as well as the piezoelectric properties of the crystal within the Density Functional Perturbation Theory (DFPT) framework [22–26]. Raman intensities have been computed ab initio for many other materials [27], even taking into account excitonic effects in the case of silicon [28], but not yet for LiIO_3 to the authors knowledge. The computation of electro-optic coefficients has been performed in Refs. [24,29–32], for LiNbO_3 , BaTiO_3 , PbTiO_3 , III–V semiconductors, Zn–IV– N_2 compounds, LiNbO_3 -type ZnGeO_2 and $\alpha\text{-GeO}_3$. However, only few of these simulation results (LiNbO_3 , BaTiO_3 and PbTiO_3) have been compared to experimental ones. As will be seen, the agreement between theoretical and experimental electro-optic tensors is not at the same level as ground-state properties. The availability of such comparison for this remarkable material, constitutes an additional benchmark for the formalism, both indicating the qualitative reliability of the methodology, but also its quantitative limits. The present study confirms numerous experimental findings and shed a new light on this piezoelectric and highly nonlinear material.

2. Calculation method

The structural properties of LiIO_3 are computed within the DFT framework using the norm-conserving Trouiller–Martins type of pseudopotential [33] generated with the `fn198FP` software [34] and using a plane-wave basis set. In this work, two exchange–correlation functionals are compared: the Perdew–Wang [35] form of the Local Density Approximation (LDA) and the Perdew–Burke–Ernzerhof parametrization of the Generalized Gradient Approximation (GGA) [36]. In both cases, the Li pseudopotential includes nonlinear core correction. The $2s^1$ electrons of Li, the $2s^2 2p^4$ electrons of O and the $5s^2 5p^5$ electrons of I are treated explicitly.

The convergence criteria for the structural properties have been set to 0.5 mHa per atom for the total energy and 0.2% of relative difference with the asymptotic value for the relaxed lattice parameters. The electronic bandstructure is considered as converged when the average difference of the eigenenergies with respect to an asymptotic band structure is less than 5 mHa. A kinetic-energy cut-off for the plane-wave basis set of 40 and 60 Ha is required in the case of LDA and GGA, respectively. A $4 \times 4 \times 4$ Monkhorst–Pack sampling [37] of the Brillouin zone is needed to achieve the desired level of convergence.

The response-function calculations relative to the lattice vibrations (phonons) and dielectric tensor are performed within DFPT. An energy cut-off of 40 Ha and a $4 \times 4 \times 4$ Monkhorst–Pack sampling is required to converge the optical tensor to 0.05%, the static permittivity and the average of Born effective charges to 1% of relative difference with respect to the asymptotic values for both functionals. A scissor shift of 0.99 eV and 1.05 eV is used for GGA and LDA to correct the intrinsic underestimation of the electronic bandgap in DFT with respect to the experimental indirect bandgap of 4.43 eV [38]. It has to be emphasized that this scissor correction has only been used for the perturbations related to the electric field.

The nonlinear properties are computed using a LDA nonlinear kernel. A $6 \times 6 \times 6$ Monkhorst–Pack sampling and a cut-off energy of 40 Ha is needed to converge the nonlinear and electro-optic tensors to 2% and 1% of the asymptotic values, respectively. To converge the Raman susceptibilities to 2% and the phonon frequencies to 1 cm^{-1} , a cut-off energy of 80 Ha and the same $6 \times 6 \times 6$ sampling are used. The same scissor shift as for linear properties

is also used for the calculations of the second-order susceptibility tensor.

Finally, the piezoelectric properties of this material have been investigated using both LDA and GGA functionals. For LDA, an energy cutoff of 60 Ha and a $4 \times 4 \times 4$ sampling are needed to converge the piezoelectric coefficients to 5% of the asymptotic values. A denser Monkhorst grid ($8 \times 8 \times 8$) as well as a higher cut-off energy (80 Ha) are required to reach same level of convergence for GGA functional.

All calculations have been done using the ABINIT software [39].

3. Results

3.1. Crystal structure and electronic bandstructure

In this section, the DFT results concerning the crystal structure and electronic bandstructure are compared with available experimental data. As already mentioned, the hexagonal phase of LiIO_3 presents the symmetry properties of the $P6_3$ spatial group. One atom of I is arbitrarily fixed at reduced position $(1/3, 2/3, 0)$. Besides the a and c lattice parameters, the crystal can be characterized by four degrees of freedom shown in Fig. 1: the position of one atom of Li along the z axis $\text{Li}_1(z)$, the position of one O atom $\text{O}_1(x, y, z)$. The bond length between O and I atoms ΔIO and the rotation angle of the IO_3 complex θ are also of interest and are also defined in Fig. 1.

The relaxed a and c values for the hexagonal lattice parameters are 5.497 Å and 5.252 Å using the GGA functional, and 5.292 Å and 4.880 Å using the LDA functional. The GGA results are in good agreement with the experimental data of 5.482 Å and 5.171 Å [7] with a maximal relative error of 1.54% whereas the LDA functional is not as good as GGA to reproduce the experimental crystal structure. More results on the atomic positions are gathered in Table 1: one can see that the internal parameters are also well reproduced in GGA except for the relative position of the Li atom which is overestimated. GGA is again in close agreement for the rotation angle of the IO_3 complex, while LDA overestimates it.

The DFT electronic band structures computed using relaxed lattice parameters and atomic positions are shown in Fig. 2 for LDA and GGA functionals. The resulting band gaps are reported

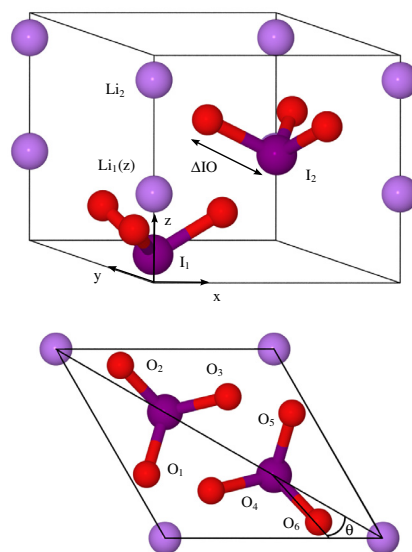


Fig. 1. Hexagonal LiIO_3 unit cell and labeling of the atoms. (Top) Labelling of the axes and I–O distance ΔIO . (Bottom) Top view of the unit cell and labeling of the rotation angle of the IO_3 complex θ .

Table 1

(Upper): DFT geometrical parameters, compared with the room temperature experimental ones. (Lower): DFT indirect Γ – K and direct K – K electronic band gaps compared to multiple experimental ones obtained at room temperature.

	Internal parameters			
	$\text{Li}_1(z)$	$\text{O}_1(x, y, z)$	$\Delta\text{IO} [\text{\AA}]$	$\theta [^\circ]$
GGA (this work)	0.4376	0.0860 0.3382 0.1615	1.84	16.3
LDA (this work)	0.4385	0.0767 0.3391 0.1814	1.78	28.5
Exp. [7]	0.3907	0.0936 0.3440 0.1698	1.82	15.8
Band gap (E_g [eV])				
Indirect				
GGA (this work)	3.44			
LDA (this work)	3.38			
GGA [31]	2.806			
Exp. [1]	4.00			
Exp. [1]	4.37			
Exp. [38]	4.43			
Direct				
GGA (this work)	3.62			
LDA (this work)	3.66			
GGA [31]	3.036			

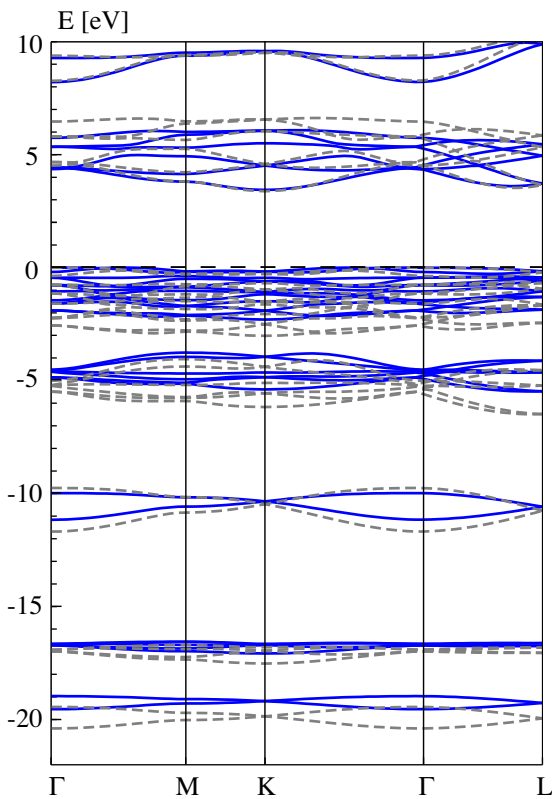


Fig. 2. Computed electronic band structure of α -LiIO₃ using (Blue) LDA and (Grey) GGA functionals. The indirect Γ – K band gaps are 3.44 eV and 3.38 eV for GGA and LDA, respectively. (For interpretation of the references to colour in this figure legend, the reader is referred to the web version of this article.)

in Table 1 and underestimate the available experimental data as expected from this level of theory [19]. One can notice that there is a difference between our results and the ones obtained by Zhang et al. [31]. The results presented in this work are in better agreement with experiments. This discrepancy may arise from different sources: pseudopotentials, convergence criteria,... The LDA and GGA band structures are in agreement for bands close to the Fermi

level with only a 0.06 eV difference on the indirect gap value. The LDA band widths are stretched with respect to the GGA ones as a result of the difference of lattice parameters.

3.2. Vibrational and dielectric properties

The linear properties obtained with DFPT are discussed in this section. The computed dielectric permittivities are reported in Table 2 and are compared with experiments. The results are improved with respect to experiments when the scissor shift is included to correct the band-gap underestimation. In the case of GGA, the theoretical optical tensor coefficients are $\epsilon_{11}^\infty = 3.56$ and $\epsilon_{33}^\infty = 3.09$. The maximal relative error with experiment is only 1.4% in this case. The GGA static permittivities are $\epsilon_{11}^0 = 9.45$ and $\epsilon_{33}^0 = 7.55$ that compares reasonably well with the experimental observations in the GHz regime [12], given the level of theoretical approximation.

The Born effective charges have been computed with both functionals and are presented in Table 3. For Li, the predicted dynamical charges for both functionals are bigger than the nominal one, especially in the xy plane. This is not the case for the I atoms, where for both functionals the effective charges are smaller than the ones of the purely ionic crystal. In the case of GGA, the effective charges are in general smaller than in the case of LDA. One can see that LDA seems to lead to a more anisotropic tensor with larger elements than GGA.

In order to compare the Born effective charges to the nominal charges, i.e. Li(+1), I(+5) and O(–2), these tensors have been symmetrized and their eigenvalues evaluated (see Table 3). Effective charges obtained by a fit to the experimental data [41] have been also reported.

Furthermore, we computed the eigenvalues of an “averaged” O Born effective charge tensor (one third of the sum of Born effective charge tensors of the three O atoms linked to one I). Thanks to symmetries, two eigenvalues $\lambda_1 = \lambda_2$ with corresponding eigenvectors (100) and (010) are thus degenerate. The resulting eigenvalues for this “averaged” effective charge tensor are then $\lambda_1 = -1.70$ and $\lambda_3 = -1.36$ for LDA, $\lambda_1 = -1.91$ and $\lambda_3 = -1.62$ for GGA.

The spread between the eigenvalues for Li, I and O reveals the strong anisotropy of the material; this also partly explains the disagreement between the computed charges and the one obtained by Cerdeira et al. [41] where only one value for the effective charge by atom was used to describe the system. Still, our results are in agreement for the charge associated to the I atom but disagree for the charge associated to the Li and O atoms.

The phonon modes at the Brillouin zone center have been classified according to their symmetries and are reported in Table 4 along with room temperature and low temperature Raman

Table 2

(Upper): The theoretical and experimental optical dielectric tensor are given. The scissor shift allows for a closer match with experiment in the THz regime. (Lower): theoretical and experimental static permittivity tensor.

	Optical tensor [/]			
	ϵ_{11}^∞	$\epsilon_{11}^\infty\text{-scis}$	ϵ_{33}^∞	$\epsilon_{33}^\infty\text{-scis}$
GGA (this work)	3.86	3.56	3.34	3.09
LDA (this work)	4.37	3.99	3.87	3.54
Exp. (THz) [40]	3.61		3.06	
Static permittivity [/]				
ϵ_{11}^0				
GGA (this work)	9.45			
LDA (this work)	10.1			
Exp. (GHz) [12]	8.2			
ϵ_{33}^0				
GGA (this work)	7.55			
LDA (this work)	8.2			
Exp. (GHz) [12]	6.4			

Table 3

(Left): Born effective charges computed using DFPT for the three atom types. The columns and rows correspond to the derivative of the energy with respect to an electric field and to an atomic displacement, respectively. The effective charges of the other O atoms can be determined using the $P6_3$ symmetry. (Right): eigenvalues of the corresponding symmetrized tensors. These values have to be compared to the nominal charges Li(+1), I(+5) and O(-2). The values from [41] are obtained by isotropic fitting to experiments.

		Born effective charges [a.u.]						Eigenvalues		Nominal	Exp. [41]	
		Tensor			Tensor							
		GGA			LDA							
		$\partial/\partial\mathcal{E}_1$	$\partial/\partial\mathcal{E}_2$	$\partial/\partial\mathcal{E}_3$	$\partial/\partial\mathcal{E}_1$	$\partial/\partial\mathcal{E}_2$	$\partial/\partial\mathcal{E}_3$					
								GGA	LDA			
Li	$\partial/\partial\tau_1$	1.45	-0.21	0.00	1.39	-0.19	0.00	λ_1	1.45	1.39	1	0.5
	$\partial/\partial\tau_2$	0.21	1.45	0.00	0.19	1.39	0.00	λ_2	1.45	1.39		
	$\partial/\partial\tau_3$	0.00	0.00	1.09	0.00	0.00	1.05	λ_3	1.09	1.05		
I	$\partial/\partial\tau_1$	3.67	0.00	0.00	4.35	-0.12	0.00	λ_1	3.67	4.35	5	3.66
	$\partial/\partial\tau_2$	0.00	3.67	0.00	0.12	4.35	0.00	λ_2	3.67	4.35		
	$\partial/\partial\tau_3$	0.00	0.00	2.98	0.00	0.00	3.83	λ_3	2.98	3.83		
O ₁	$\partial/\partial\tau_1$	-1.33	-0.26	0.34	-1.65	-0.35	0.52	λ_1	-1.32	-1.465	-2	-1.39
	$\partial/\partial\tau_2$	-0.40	-2.08	0.23	-0.55	-2.18	0.38	λ_2	-2.55	-3.03		
	$\partial/\partial\tau_3$	0.50	0.80	-1.36	0.75	0.96	-1.63	λ_3	-0.91	-0.97		

Table 4

Phonon frequencies classified according to their symmetry representation. Experimental data obtained at room temperature [42] and at 10 K [43] are also shown.

	Phonon frequencies (cm ⁻¹)			
	GGA	LDA	Exp. [42]	Exp. [43]
A(TO-LO)	155–155 170–188 338–439 718–750	192–196 248–248 354–468 730–787	148 238 358–468 795–817	157–159 237–243 360–470 791.5–817
E ₁ (TO-LO)	165–170 298–311 313–415 690–772	199–203 337–355 378–462 694–805	180 330–340 370–460 769–848	178–183 332–340 /-455 765–844
E ₂	75 202 256 325 686	129 230 318 353 702	98 200 332 347 765	102.3 212 292 346.5 761
B	138 181 367 451 748	165 234 401 533 782	/	/

measurements. Some disagreements at low and high frequencies can be pinpointed but can be partially explained by temperature effects or by the use of pseudopotentials. There is on average a difference of 5.74% for LDA and of 9.9% for GGA. In the case of phonons, LDA pseudopotentials seem to perform better than GGA ones for LiO₃. The B modes are silent in both infrared and Raman experiments, hence our data are predictions for these frequencies.

In addition, the infrared reflectivity spectra has been investigated using the dielectric permittivity [23,42]:

$$\epsilon_{\alpha\beta}(\omega) = \epsilon_{\alpha\beta}^{\infty} + \frac{4\pi}{\Omega_0} \sum_m \frac{S_{m\alpha\beta}}{\omega_m^2 - \omega^2 + i\omega\Gamma_m}, \quad (1)$$

where ω is the incoming photon frequency, Ω_0 is the volume of the unit cell, m is the index of the phonon mode, $S_{m\alpha\beta}$ is the oscillator strength tensor related to the mode m , ω_m the phonon frequency and Γ_m the damping factor related to the phonon lifetime. From this expression, the reflectivity can be deduced for an electric field aligned with the direction k :

$$R_k = \left| \frac{\epsilon_{kk}^{1/2} - 1}{\epsilon_{kk}^{1/2} + 1} \right|^2. \quad (2)$$

In order to reproduce experimental data, the same mode-dependent phonon lifetimes as the ones proposed by Otaguro and Wiener-Avneer [42] have been used (ranging from 12 to 60 cm⁻¹). The computed reflectivities shown in Fig. 3 for both functionals are in good agreement for most of the spectrum except for the high frequency part. One should notice that the simulations are done at fixed ion equilibrium positions while experiments are done at non-zero temperature.

3.3. Raman spectra and nonlinear coefficients

The polarization can be decomposed into a Taylor series of the electric field \mathcal{E}_j [24]:

$$P_i = P_i^S + \sum_j \chi_{ij}^{(1)} \mathcal{E}_j + \sum_{j,k} \chi_{ijk}^{(2)} \mathcal{E}_j \mathcal{E}_k + \dots, \quad (3)$$

where P_i^S is the spontaneous polarization of the material, $\chi_{ij}^{(1)}$ is the linear dielectric susceptibility (which has been computed in the previous section) and $\chi_{ijk}^{(2)}$ is the second-order optical susceptibility. The nonlinear tensor d_{ijk} is defined as

$$d_{ijk} = 2\chi_{ijk}^{(2)}, \quad (4)$$

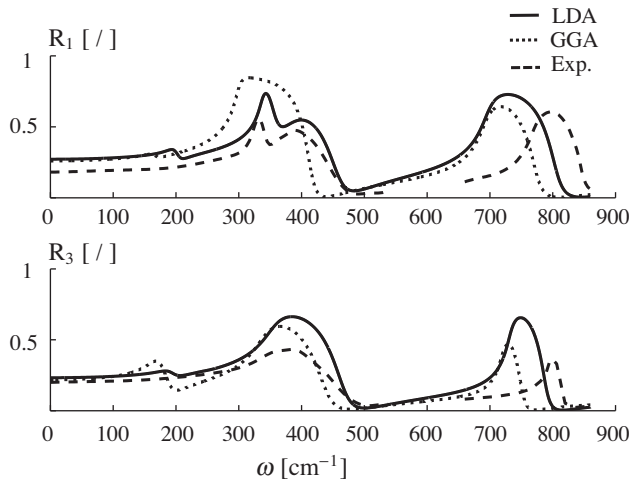


Fig. 3. Computed reflectivity spectra with an incident light along the (upper panel) x axis, and (lower panel) z axis, obtained within the framework of DFPT, in the infrared regime. The continuous line, the dashed line and the dotted line correspond to the results using LDA, GGA and to the experimental data [42], respectively.

and its components are summarized in Table 5. As for the case of linear properties, the inclusion of a scissor shift improves the agreement with experiment. The discrepancy between the theoretical and the experimental value of d_{33} can be explained by the underestimation of the c lattice parameter by the LDA functional.

Finally, the static limit of the Raman scattering of α -LiIO₃ is presented. The Raman scattering efficiencies $dS/d\Omega$ for each phonon mode can be obtained from the following equation [24]:

$$\frac{dS}{d\Omega} = \frac{(\omega_0 - \omega_m)^4}{c^4} |\mathbf{e}_s \cdot \boldsymbol{\alpha}_m \cdot \mathbf{e}_0|^2 \frac{\hbar}{2\omega_m} (n_m + 1), \quad (5)$$

where ω_0 is the laser frequency, ω_m is the frequency of phonon mode m , \mathbf{e}_s and \mathbf{e}_0 are the polarizations of incoming and outgoing electromagnetic waves, respectively, n_m the Bose–Einstein distribution function, $\boldsymbol{\alpha}_m$ the Raman susceptibility and Ω is the angle of collection in which the outgoing photon is scattered. The Raman intensity is defined as $I = C dS/d\Omega$ where C is constant. Traditionally, in the literature, the Raman intensities are presented in arbitrary units: we will therefore always present I/I_{\max} .

The Raman susceptibility corresponds to the variation of the dielectric permittivity with the atomic position perturbation created by the phonon and can be computed in the static limit using DFPT [24]. This tensor takes different forms depending on the mode symmetry [42]:

$$A(z) = \begin{pmatrix} \alpha_1 & 0 & 0 \\ 0 & \alpha_1 & 0 \\ 0 & 0 & \alpha_2 \end{pmatrix},$$

$$E_1(x) = \begin{pmatrix} 0 & 0 & \alpha_1 \\ 0 & 0 & \alpha_2 \\ \alpha_1 & \alpha_2 & 0 \end{pmatrix}, \quad E_1(y) = \begin{pmatrix} 0 & 0 & -\alpha_2 \\ 0 & 0 & \alpha_1 \\ -\alpha_2 & \alpha_1 & 0 \end{pmatrix}$$

$$E_2 = \begin{pmatrix} \alpha_1 & \alpha_2 & 0 \\ \alpha_2 & -\alpha_1 & 0 \\ 0 & 0 & 0 \end{pmatrix}, \quad E_2 = \begin{pmatrix} \alpha_2 & -\alpha_1 & 0 \\ -\alpha_1 & -\alpha_2 & 0 \\ 0 & 0 & 0 \end{pmatrix}$$

while for E_2 modes, one has to notice that only the sum of the square of these coefficients have a physical meaning. The corresponding values of these coefficients are reported in Table 5.

The phonon lifetime which contributes to a broadening of the Raman peak in the spectrum are not taken into account in this

Table 5

(Top) Computed and experimental nonlinear tensor coefficients d_{31} and d_{33} . Experiments from [14] performed with a laser wavelength of 2.12 μm . (Bottom) Phonon frequencies and their Raman susceptibilities classified according to their symmetry. 10^{-3} a.u. corresponds to 7.6218×10^6 (m/kg)^{1/2} in SI units.

		Nonlinear coefficients (pm/V)			
		d_{31}	$d_{31\text{-scis}}$	d_{33}	$d_{33\text{-scis}}$
LDA (this work)		-9.9	-6.6	-11.2	-7.5
Exp. [14]			-6.43		-6.41
		Raman susceptibilities (10^{-3} a.u.)			
		ω (TO–LO)	α_1		α_2
		TO	LO	TO	LO
A	192–196	-3.3	-2.3	-2.8	-1.4
A	248–248	4.4	4.3	5.5	5.9
A	354–468	4.9	4.6	8.55	6.2
A	730–787	2.6	-2.2	2.2	1.8
E_1	199–203	-1.8	-0.4	-1.7	-1.5
E_1	337–355	-1.1	7.7	-0.3	5.9
E_1	378–462	-1.5	-1.4	-3.3	-3.4
E_1	694–805	-4.7	-12	-3.9	-7.6
	ω	α_1		α_2	
E_2	129		2.2		1.2
E_2	230		-0.6		0
E_2	318		-1.1		0.3
E_2	353		-3.1		3.5
E_2	702		-2.5		5.0

simulation, we propose Dirac delta functions located at phonon frequencies. These delta functions are weighted by the theoretical intensities.

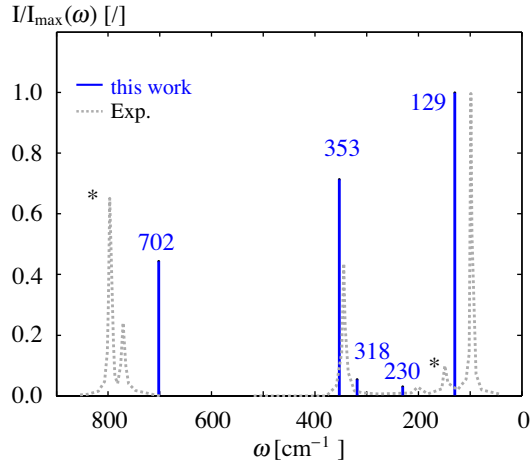
The available experimental Raman spectra are obtained with a laser frequency ω_0 of 514.5 nm at either 12 K or 298.15 K [42,43]. The computed Raman spectra are presented in Figs. 4 and 5, where the notation $h(ij)k$ refers to the propagation directions of the incident and scattered photons through h and k , respectively and to their polarization through i and j .

In this section, we will discuss the theoretical peak intensities. First, the spectrum for E_2 modes is in qualitative agreement with the experiment (Fig. 4) and the relative intensities are very well reproduced. The changes of intensities related to the broadening can be the reason of the quantitative disagreement.

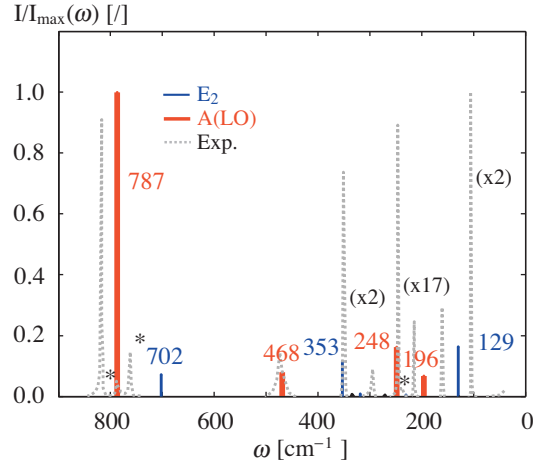
For the A(TO) modes (Fig. 4b), the agreement between experiments and theory is less convincing. The high frequency peak is the most important in both cases but for low frequencies the relative intensities deviates, even qualitatively, from experiments. Similar conclusions apply for the A(LO) + E_2 modes (Figs. 4c and 5a) where the 787 cm^{-1} mode intensity seems to be overestimated. However, the other modes are in qualitative agreement with experiments. The theoretical spectrum for the E_1 modes (Fig. 5b) matches relatively well the experimental one.

The differences between the results of this work and the experiments could come from different sources: the relaxed lattice parameter c mismatch, the temperature effect (broadening of the peaks) or the fact that the laser frequency is not negligible compared to the band gap and thus could lead to pre-resonance effects. Finally, large discrepancies are observed between different experimental room temperature results for measured relative Raman intensities [42–45]. For example, Otaguro et al. assigned the third E_2 mode to 332 cm^{-1} while Melo and Cerdeira reported 342 cm^{-1} and 346 cm^{-1} .

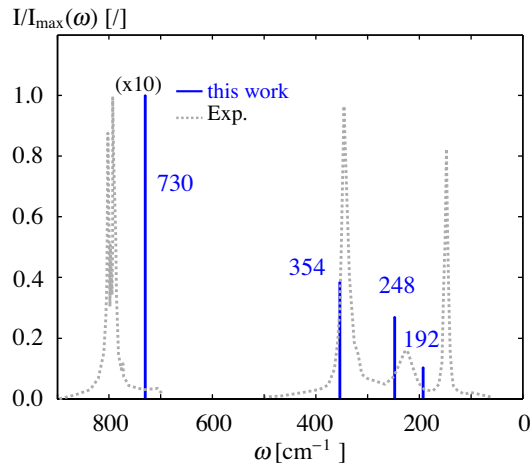
The electro-optic (EO) effect or Pockels effect corresponds to the modification of refractive index due to the application of an external electric field. It is characterized by the linear EO coefficients r_{ijk} :



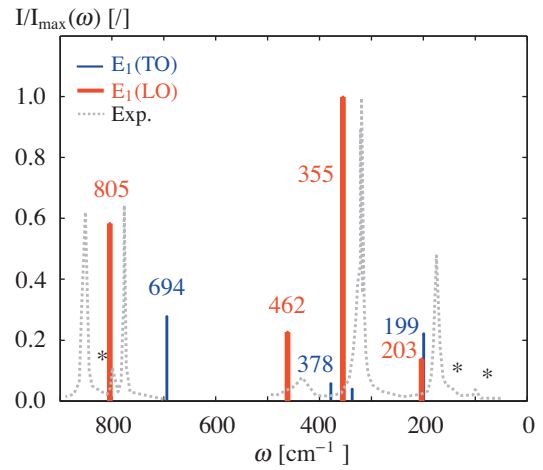
(a) Raman spectrum for the X(YX)Y configuration (Blue) E_2 modes.



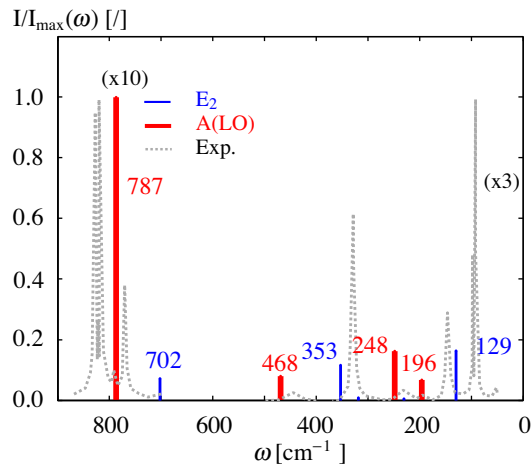
(a) Raman spectrum for the X(ZX)Y. (Blue) E_2 modes (Red) A(LO) modes. Experimental measurements have been performed at 12K [43].



(b) Raman spectrum for the X(ZZ)Y configuration. (Blue) A(TO) modes.



(b) Raman spectrum for Z(YY)Z configuration. (Blue) E_1 (TO) modes (Red) E_1 (LO) modes. Measures have been performed at room temperature[42].



(c) Raman spectrum for the X(ZX)Y configuration. (Blue) E_2 modes (Red) A(LO) modes.

Fig. 4. Theoretical Raman spectra obtained by DFPT and comparison with experimental data. Measures have been performed at room temperature [42]. Artifacts from crystal misorientation are reported by an asterisk while zooms are reported as (x γ) where γ is the magnification.

Fig. 5. Theoretical Raman spectra obtained by DFPT and comparison with experimental data. configuration. Artifacts from crystal misorientation are reported by an asterisk while zooms are reported as (x γ) where γ is the magnification.

$$\Delta(\epsilon^{-1})_{ij} \triangleq \sum_k r_{ijk} \mathcal{E}_k \quad (6)$$

where \mathcal{E}_k is a low-frequency or static electric field. In hexagonal LiIO_3 , there are 4 independent electro-optic coefficients (in Voigt notation): r_{11} , r_{33} , r_{41} and r_{42} . This response can be decomposed into three contributions [11]: an electrical part, an ionic one and a piezoelectric one. In this work, we examine the case of clamped cells: the cell parameters are not allowed to change as the electric field is applied. The piezoelectric contribution thus vanishes. Experimentally, it corresponds to an applied electric field of frequency above ≈ 100 MHz [24].

The electro-optic coefficients for the clamped case r_{ij}^S are reported in Table 6 along with the experimental data. The predicted mode by mode decomposition and electronic contribution are also presented.

Table 6

(Upper): Decomposition of the clamped electro-optic tensor for hexagonal LiIO₃. The contributions of each zone-center phonon modes as well as the electronic contribution are reported. Experimental data available at room temperature and for high frequencies (above the acoustic resonances) are also presented. (Lower): theoretical electro-optic coefficients for LiNbO₃, PbTiO₃, BaTiO₃ and experimental data from the literature.

Electro-optic coefficients (pm/V)						
A modes			E ₁ modes			
ω	r_{31}^S	r_{33}^S	ω	r_{41}^S	r_{42}^S	
TO ₁	192	0.81	0.88	199	0.56	-0.12
TO ₂	248	-0.17	-0.31	337	0.46	3.10
TO ₃	354	2.04	4.56	378	0.46	-0.44
TO ₄	730	1.97	2.07	694	-0.66	1.70
El.		2.09	3.02		0.00	2.36
Tot.		6.75	10.22		0.82	6.60
Exp. [11]		4.1 ± 0.6	6.4 ± 1		1.4 ± 0.2	3.3 ± 0.7
Exp. [42]		5.8 ± 1.2				

Electro-optic coefficients (pm/V)					
		r_{31}^S	r_{33}^S	r_{22}^S	r_{51}^S
LiNbO ₃	LDA [24]	9.67	26.93	4.55	14.93
	Exp. [1]	8.6	30.8	3.4	28
PbTiO ₃	LDA [24]	8.98	5.88		30.53
	Exp. [46]	13.8	5.9		
BaTiO ₃	LDA [24]	8.91	22.27		
	Exp. [47]	10.2	40.6		
	Exp. [1]	8	28		

One can see that only the A modes couple to r_{31}^S and r_{33}^S while only the E₁ modes contribute to r_{41}^S and r_{42}^S . The negligible electronic contribution to the EO coefficient r_{41}^S is also noticeable. Each mode contributes to the electro-optic effect, especially the mode A(TO₃) to r_{33}^S and the mode E₁(TO₂) to r_{42}^S . The results approach the experimental results from Ref. [11] with a maximal relative difference of 40%.

For comparison, EO coefficients for ferroelectric materials (LiNbO₃, PbTiO₃ and BaTiO₃) obtained with the same ab initio technique [24] are reported in Table 6 as well as the corresponding experimental data. Although good agreements are obtained for r_{33}^S (PbTiO₃) and r_{31}^S (BaTiO₃), larger discrepancies ($\approx 47\%$) are observed for r_{33}^S (BaTiO₃) and r_{51}^S (LiNbO₃).

The difference between experiments and theory may come from multiple sources. First, the results depend on the choice of pseudopotentials. Secondly, the lattice parameter c is underestimated in our simulation and the optical dielectric constant overestimated. Thirdly, the computation are performed at fixed ion position while experimental values are obtained at room temperature.

Finally, it has to be emphasized that the experimental measurements of the EO coefficients are extremely sensitive to the temperature [48] as well as to the stoichiometry of the crystal and its defect concentration [49]. As LiIO₃ properties strongly depend on the crystal growth conditions [50], variations of the EO coefficients are thus expected between specimen grown from different conditions, although no study on this topic have been performed to the authors knowledge. This computation provides a prediction of the EO coefficients for pure hexagonal LiIO₃ crystal. The predictive power of this technique is then limited by the previously cited factors.

3.4. Piezoelectric properties

The electric displacement field is linked to the strain η_j and to the electric field \mathcal{E}_j by the following formula:

$$D_i = \sum_j e_{ij} \eta_j + \sum_j \epsilon_{ij} \mathcal{E}_j \quad (7)$$

Table 7

Computed piezoelectric tensors for both LDA and GGA functionals as well as experimental data available.

	Piezoelectric tensor (C/m ²)			
	e_{13}	e_{33}	e_{41}	e_{42}
LDA (this work)	1.14	1.54	-0.13	1.26
GGA (this work)	0.92	1.28	-0.07	1.10
Exp. [51]	0.65	0.97	0.10	0.89

where e_{ij} is the piezoelectric tensor. In the case of hexagonal LiIO₃, the piezoelectric tensor has only 4 nonzero components: e_{13} , e_{33} , e_{41} and e_{42} . They are reported in Table 7 for both LDA and GGA functionals and compared with the experimental data available.

GGA and LDA reproduce the experimental tendencies but overestimate the piezoelectric coefficients. Nevertheless, one can notice that GGA lies closer to experiment than LDA.

4. Conclusions

In this work, first-principle simulations of linear and nonlinear properties of α -LiIO₃ are performed. First of all, the lattice parameters reproduce experiment within 1.57% using a GGA functional. Linear properties of LiIO₃ are well reproduced using DFPT techniques. For instance, the optical tensor coefficients in GGA match experimental results (within 2%) when a scissor shift is used and the reflectivity is well reproduced for a wide range of frequencies in the infrared regime.

For nonlinear properties, the second-order dielectric susceptibility tensor presents a similar agreement (2.6% of error). Qualitative agreement on the Raman spectra is noticed. However, there is still room for future works since many effects can affect the results such as the first-principle inclusion of the temperature dependence [52].

Tendencies for the EO coefficients are reproduced and the agreement with experiments is similar to other works where relative differences can reach value as high as 50%.

Acknowledgments

The authors would like to thank Yann Pouillon and Jean-Michel Beuken for their valuable technical support and help with the test and build system of ABINIT as well as Matteo Giantomassi for technical support. This work is supported by the FRS-FNRS through a FNRS (Y.G.) and a FRIA grant (S.P.). Computational resources have been provided by the supercomputing facilities of the Université catholique de Louvain (CISM/UCL) and the Consortium des Équipements de Calcul Intensif en Fédération Wallonie Bruxelles (CÉCI) funded by the Fonds de la Recherche Scientifique de Belgique (F.R.S.-FNRS) under convention 2.5020.11.

References

- [1] D.N. Nikogosyan, *Rarely Used and Archive Crystals*, Springer, New York, 2005.
- [2] G. Nath, H. Mehmanesch, M. Gsänger, *Appl. Phys. Lett.* 17 (1970) 286.
- [3] U. Deserno, G. Nath, *Phys. Lett. A* 30 (1969) 483.
- [4] W.P. Risk, T.R. Gosnell, A.V. Nurmikko, *Compact Blue-Green Lasers*, Cambridge University Press, 2003.
- [5] R.C. Miller, W.A. Nordland, *Phys. Rev. B* 2 (1970) 4896.
- [6] W.H. Zachariasen, F.A. Barta, *Phys. Rev.* 37 (1931) 1626.
- [7] A. Rosenzweig, B. Morosin, *Acta Crystallogr.* 20 (1966) 758.
- [8] J. Liebertz, *Zeit Phys. Chem.* 67 (1969).
- [9] H. Arend, M. Remoissenet, W. Staehlin, *Mater. Res. Bull.* 7 (1972) 869.
- [10] V. Lemos, J.M. Filho, F.E.A. Melo, R.S. Katiyar, F. Cerdeira, *Phys. Rev. B* 28 (1983) 2985.
- [11] F.R. Nash, J.G. Bergman, G.D. Boyd, E.H. Turner, *J. Appl. Phys.* 40 (1969) 5201.
- [12] A.W. Warner, D.A. Pinnow, *J. Acoust. Soc. Am.* 47 (1970) 791.
- [13] J. Jerphagnon, *Appl. Phys. Lett.* 16 (1970) 298.
- [14] M.M. Choy, R.L. Byer, *Phys. Rev. B* 14 (1976) 1693.
- [15] R.C. Eckardt, H. Masuda, Y.X. Fan, R.L. Byer, *IEEE J. Quant. Electr.* 26 (1990) 922.
- [16] R. Gehr, A. Smith, *J. Opt. Soc. Am. B* 15 (1998) 2298.

- [17] W. Alford, A. Smith, *J. Opt. Soc. Am. B* 18 (2001) 524.
- [18] Y. Gang, C. Yu, A. Xin-You, J. Zhong-Qian, C. Lin-Hong, W. Wei-Dong, Z. Yan, *Chin. Phys. Lett.* 30 (2013) 067101.
- [19] R.M. Martin, *Electronic Structure, Basic Theory and Practical Methods*, Cambridge University Press, 2004.
- [20] Y. Wang, J. Perdew, *Phys. Rev. B* 44 (1991) 13298.
- [21] D. Hamann, M. Schluter, C. Chiang, *Phys. Rev. Lett.* 43 (1979) 1494.
- [22] X. Gonze, *Phys. Rev. B* 55 (1997) 10337.
- [23] X. Gonze, C. Lee, *Phys. Rev. B* 55 (1997) 10355.
- [24] M. Veithen, X. Gonze, P. Ghosez, *Phys. Rev. B* 71 (2005) 125107.
- [25] D.R. Hamann, X. Wu, K.M. Rabe, D. Vanderbilt, *Phys. Rev. B* 71 (2005) 035117.
- [26] X. Wu, D. Vanderbilt, D.R. Hamann, *Phys. Rev. B* 72 (2005) 035105.
- [27] R. Caracas, E. Bobocioiu, *Am. Mineral.* 96 (2011) 437. WURM database <<http://wurm.info/>>.
- [28] Y. Gillet, M. Giantomassi, X. Gonze, *Phys. Rev. B* 88 (2013) 094305.
- [29] E. Roman, J.R. Yates, M. Veithen, D. Vanderbilt, I. Souza, *Phys. Rev. B* 74 (2006) 245204.
- [30] T.R. Paudel, W.R.L. Lambrecht, *Phys. Rev. B* 79 (2009) 245205.
- [31] J. Zhang, B. Xu, Z. Qin, X. Li, K. Yao, *J. Alloy Compd.* 514 (2012) 113–119.
- [32] P. Hermet, G. Fraysse, A. Lignie, P. Armand, P. Papet, *J. Phys. Chem. C* 116 (2012) 8692–8698.
- [33] N. Troullier, J.L. Martins, *Phys. Rev. B* 43 (1991) 1993.
- [34] M. Fuchs, M. Scheffler, *Comput. Phys. Commun.* 119 (1999) 67.
- [35] J.P. Perdew, Y. Wang, *Phys. Rev. B* 45 (1992) 13244.
- [36] J.P. Perdew, K. Burke, M. Ernzerhof, *Phys. Rev. Lett.* 77 (1996) 3865.
- [37] H.J. Monkhorst, J.D. Pack, *Phys. Rev. B* 13 (1976) 5188.
- [38] K. Wu, C. Chen, *J. Cryst. Growth* 166 (1996) 533.
- [39] X. Gonze, B. Amadon, P.-M. Anglade, J.-M. Beuken, F. Bottin, P. Boulanger, F. Bruneval, D. Caliste, R. Caracas, M. Côté, T. Deutsch, L. Genovese, P. Ghosez, M. Giantomassi, S. Goedecker, D. Hamann, P. Hermet, F. Jollet, G. Jomard, S. Leroux, M. Mancini, S. Mazevet, M. Oliveira, G. Onida, Y. Pouillon, T. Rangel, G.-M. Rignanese, D. Sangalli, R. Shaltaf, M. Torrent, M. Verstraete, G. Zerah, J. Zwanziger, *Comput. Phys. Commun.* 180 (2009) 2582.
- [40] S.K. Kurtz, T.T. Perry, *Appl. Phys. Lett.* 12 (1968) 186.
- [41] F. Cerdeira, V. Lemos, F.E.A. Melo, M. Cardona, *Phys. Status Solidi B* 122 (1984) 53.
- [42] W. Otaguro, E. Wiener-Avneer, *Phys. Rev. B* 4 (1971) 4542.
- [43] F. Cerdeira, F. Melo, V. Lemos, *Phys. Rev. B* 27 (1983) 7716.
- [44] F.E.A. Melo, F. Cerdeira, *Phys. Rev. B* 26 (1982) 720.
- [45] Y. Du, Y. Sun, W.C. Chen, X.L. Chen, L.N. Zhu, *Int. J. Mod. Phys. B* 21 (2007) 4495.
- [46] M.J. Weber, *Handbook of Laser Science and Technology Supplement 2: Optical Materials*, CRC Press, 1994.
- [47] M. Zgonik, P. Bernasconi, M. Duelli, R. Schlessler, P. Günter, M.H. Garrett, D. Rytz, Y. Zhu, X. Wu, *Phys. Rev. B* 50 (1994) 5941.
- [48] M. Aillerie, M. Fontana, F. Abdi, C. Carabatos-Nedelec, N. Theofanous, G. Alexakis, *J. Appl. Phys.* 65 (1989) 2406.
- [49] M. Aillerie, K. Chah, F. Abdi, P. Bourson, M. Fontana, K. Polgar, G. Malovichko, *Ferroelectrics* 223 (1999) 365.
- [50] Z. Mai, H. Guo, W. Chen, G. Luo, Y. Wu, G. Zhai, C. Wang, Y. Zhu, *Solid State Commun.* 101 (1997) 443.
- [51] S. Haussühl, *Acta Acust.* 23 (1970) 165.
- [52] S. Poncé, G. Antonius, P. Boulanger, E. Cannuccia, A. Marini, M. Côté, X. Gonze, *Comput. Phys. Commun.* 83 (2014) 341.